

Microneedle Penetrating Array with Axon-Sized Dimensions for Cuff-less Peripheral Nerve Interfacing

Dongxiao Yan, Ahmad Jiman, David Ratze, Shuo Huang, Saman Parizi, Elissa Welle, Zhonghua Ouyang,
Paras Patel *Member IEEE*, Mark J. Kushner *Fellow IEEE*, Cynthia Chestek *Member IEEE*,
Tim M. Bruns *Member IEEE*, Euisik Yoon, *Member IEEE*, John Seymour *Member IEEE*

Abstract— Autonomic nerves are typically only hundreds of microns in diameter near their organ targets and these carry all of the sympathetic and parasympathetic control signals. We present a cuff-less microneedle array specifically designed to potentially map small autonomic nerves. The focus of this paper is the design and fabrication of an ultra-miniaturized silicon needle array on a silicone substrate. We demonstrate arrays having 25 to 100 microneedles. Each needle has a 1-micron tip and dual-taper shaft. We demonstrate an ability to control the tip shape, angle, and shaft angle which is important for balancing sharpness and stiffness. These high-density arrays also include a special backside anchor embedded in silicone for stability in the elastic substrate, yet the array freely wraps over a 300-μm nerve. Another critical method presented here is a surgical technique for inserting and securing an array without a cuff (as small as 0.3 mm wide and 1.2 mm long) by photochemical bonding of collagen/Rose Bengal adhesive agents to epineurium. Future work will focus on device functionalization and histological characterization in a rat vagus model.

I. INTRODUCTION

Implantable peripheral nerve interfaces can be categorized as cuff (surrounding the epineurial surface), intrafascicular (through the perineurium), and regenerative (bridging two nerve ends). Cuff devices do not have the ability to detect individual or local axon activity through the highly resistive epineurium and thus lack spatial resolution. Intrafascicular arrays, by contrast, implant electrodes transversely or longitudinally to the nerve and may have significant tissue damage. Even thin polymer arrays, which for the last decade represent the state-of-the-art in this field, result in tissue encapsulation around the microelectrodes on the order of 50–100 μm [1]. While an improvement over past technologies such as the high-density Utah electrode array (HD-UEA) [2] which showed excellent longevity for stimulation in larger nerves, flexible polymer arrays are greatly oversized for most autonomic nerves, which are often below 1 mm in diameter.

The goal of Microneedle Nerve Array (MINA) is to offer a minimally invasive intrafascicular penetrating technology that ideally extends just beyond the epineurium and perineurium of a fascicular bundle and with recording needles similar in size to large axons (~20 μm). We hypothesize that the size of each individual penetrating structure is a critical factor influencing the tissue response. Additionally, the way in which the array is secured to the nerve is also a critical factor.

II. METHODS

Each individual penetrating microneedle of MINA has a total height of 180 μm. As they are anchored onto the neutral plane of an 80-μm thick PDMS layer, the exposed needle bodies have an average length of 140 μm. The average diameter of the needle tip and whole needle body is 6.3 μm and 17.6 μm. Table I shows a comparison of the individual needle diameter of MINA with the current state-of-the-art silicon needle array, HD-UEA. As shown in Figure 1, the ultra-fine silicon microneedles were placed in a honeycomb pattern with 150 μm spacing.

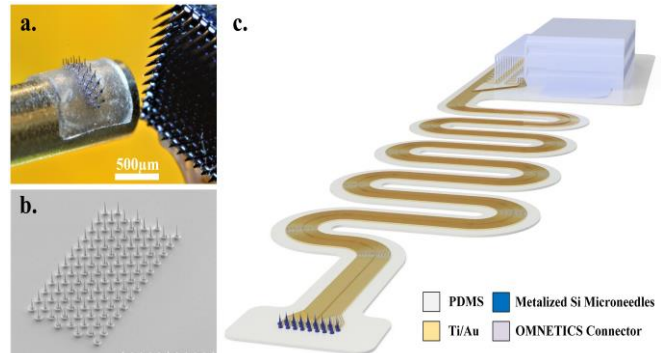


Figure 1. Microneedle Nerve Array (MINA). a. Size comparison between MINA and high-density Utah slant array. MINA wrapped around a metal rod (0.56-mm diameter). b. SEM image of 100-site silicon microneedle array in a 0.9mm x 1.8mm rectangular area. c. Conceptual image of a future functional version of MINA.

A. Axon-Dimension Microneedle Design, Simulation and Microfabrication

The process of scaling down the cross-section of the penetrating structures requires careful design to ensure mechanical robustness. A ~10μm diameter high-aspect-ratio silicon structure can be extremely fragile during penetration or while implanted. To optimize the structural mechanics of the ultra-fine silicon microneedle, we used finite element methods (FEM) in COMSOL to evaluate tip angles and shaft angles while trying to keep the upper portion in particular smaller than a large axon diameter (< 20 μm). A dual-taper-profile (i.e. a full tip angle of 30° degrees and a shaft side-wall angle of 3°)

Research supported by NIH SPARC, Award OT2OD024907
D. Yan (yando@umich.edu), D. Ratze, S. Huang, S. Parizi, M. Kushner (mjkush@umich.edu), E. Yoon (esyoon@umich.edu), J. Seymour (seymourj@umich.edu) are with the University of Michigan Department of Electrical Engineering & Computer Science, Ann Arbor, MI, 48109 USA

A. Jiman (ajman@umich.edu), E. Welle, Z. Ouyang, P. Patel, C. Chestek (cchestek@umich.edu), T.M. Bruns (bruns@umich.edu) are with the University of Michigan Department Of Biomedical Engineering and the Bionterfaces Institute, Ann Arbor, MI, 48109 USA.

Corresponding author is J. Seymour (e-mail: seymourj@umich.edu).

with a cylindrical backside anchor provided us with the greatest stability inside the soft bulk material of the array body.

The yield stress of silicon is around 7 GPa. Simulation using COMSOL predicted a maximum stress of only 13.4 MPa under 1 gram force applied both lateral and longitudinal on a nerve phantom laying over the top of the needle with non-slip boundary condition. (Figure 2) The Young's module of the nerve was set at 300 kPa.

TABLE I. NEEDLE SIZE COMPARISON OF MINA VS HD-UEA

Device	Average Diameter at % Distance to the Tip (μm)			
	5%	20%	50%	90%
MINA	4.3	13.3	16.9	24.2
HD-UEA	-	41.2	73.3	107.3

Deep reactive ion etching (DRIE) of silicon creates a negative sidewall angle unsuitable for microneedles if a modification is not introduced. In our case we used a thin, protective ring to create a micro-loading effect in the etch around our needles (Figure 3), which is a modified approach from Hanein 2003 [3]. A computational study of DRIE of silicon microneedles was conducted to improve our understanding of the etching and resulting sidewall profiles. We modeled the fabrication process in two steps: reactor scale modeling of the inductively coupled plasma (ICP) providing reactive fluxes to the substrate and single microneedle scale etching process simulation. The reactor scale modeling was performed using the Hybrid Plasma Equipment Model (HPEM), from which the neutral and ion fluxes and ion energy and angular distributions (IEADs) to the wafer surface were obtained [4]. The resulting microneedle profiles were predicted using the Monte Carlo Feature Profile Model (MCFPM) [5].

MINA was fabricated starting with a Silicon on Insulator (SOI) wafer where the buried oxide layer depth defines the desired needle length. A silicon dioxide hard mask was deposited and patterned through lithography and oxide etching. Next the silicon was etched in a series of isotropic-anisotropic-isotropic conditions. The buried oxide layer was used as an etch-stop layer. High-quality insulation of the silicon was grown using thermal oxidation. Future versions of the microneedle electrode will require tip etching, metallization, and interconnection. Next, silicone was formed over the needles. Specifically, 1:1 diluted 20:1 PDMS (Sylgard 184) was spun over the microneedle arrays. Next, a PDMS stamp was pressed over the arrays to improve planarity of the uncured silicone. The wafer was then temporarily bonded onto a glass wafer to protect the topside. Finally, the handling layer of the SOI wafer was dissolved in 20% KOH solution and the arrays were released.

B. Photochemical Device-Epineurium Bonding Agent

Collagen (C9791 Sigma) and Rose Bengal (330000 Aldrich) were dissolved in 30% ethanol separately at 0.1 wt%. Then the collagen ethanol solution was ultrasonicated for 10 min at room temperature. Next, the collagen and RB ethanol solution were mixed at a 10:1 ratio. Next, the device was treated by oxygen plasma for surface activation. Oxygen plasma generated Si-O- groups on the silicone surface to bond

with collagen matrices. The obtained collagen/RB ethanol solution was drop-cast onto the MINA surface shortly after plasma exposure. Finally, the devices were air-dried at 50°C and sterilized using low-temperature (37.7°C) ethylene oxide (EtO).

C. Surgical Method to Access Cervical Vagus Nerve

All experimental procedures were approved by the University of Michigan Institutional Animal Care and Use Committee. Experiments were performed on female 220-270 g Sprague-Dawley rats (Charles Rivers Laboratories). One day prior to surgery, animals were injected subcutaneously with dexamethasone (0.2 mg/kg). For the implant procedure, animals were anesthetized with isoflurane (1-5%) and injected subcutaneously with carprofen (5 mg/kg), lidocaine (0.4%), and dexamethasone (0.20 mg/kg). A midline cervical incision was made to access the right cervical vagus nerve. Under a dissection microscope (Lynx EVO, Vision Engineering Inc.), the vagus nerve was isolated (5-7 mm) from the carotid artery and surrounding tissue and placed on a custom 3D-printed nerve holder (Figure 4). MINA was held on a custom vacuum adapter connected to a micromanipulator for accurate placement. A small pencil-shaped camera (MS100, Teslong) was positioned in the surgical opening to allow for visualization of device implantation.

D. Cuff-less Technique for MINA implantation

The key to achieving cuff-free implantation was the novel photochemical bonding of the nerve epineurium to the surface of the MINA. This approach was inspired by previous work demonstrating a Rose Bengal-chitosan patch as a means to adhere two halves of tissue [6]. Previously, Rose Bengal was demonstrated as a suture-less wound closure technique [7] and more recently for nerve grafting [8]. The mechanism of action is covalent cross-linking of collagen molecules facilitated by light activation of Rose Bengal (a fluorescein-like molecule). Light activation at the MINA/nerve interface was by a laser beam (532 nm, 85 mW) for 2-3 minutes. A 0.8-mm diameter beam was positioned along MINA on 3-4 spots, moving to new position every two seconds. Saline was periodically rinsed over the nerve to dissipate heat after laser exposure. After adhesion, the vagus nerve was removed from the nerve holder and surgical clips were used to close the skin incision. A subcutaneous injection of carprofen (5 mg/kg) and dexamethasone (0.2-0.05 mg/kg) were administered daily after surgery for 2-3 days. Animal's health was checked daily.

E. Terminal Electrophysiology Assessment

A terminal procedure under isoflurane anesthesia (1-5%) was performed to assess nerve function prior to sample removal for imaging. A bipolar cuff electrode (0.75 mm inner-diameter, Microprobe for Life Science,) was placed on the vagus nerve distal to the implant region to record neural activity (PowerLab, ADInstruments). A stimulation probe was placed on the vagus nerve proximal to the implant region and connected to an isolated pulse generator (Model 2100, A-M Systems). Electrical stimulation (1-8 mA, 2 Hz) was applied to evoke neural activity. After testing animals were euthanized with an overdose of sodium pentobarbital (400 mg/kg). The implanted nerves were extracted and kept in 3% glutaraldehyde.

F. Micro-CT Imaging

Microscopic X-Ray Computed Tomography (micro-CT, Zeiss Versa 520), where X-rays are emitted from an X-ray generator, travel through a rotating nerve sample, and are recorded by a detector on the other side to produce a radiograph series, was used to visualize chronic MINA nerve implants. By varying the focus depth, the 3D tomography was constructed from 2.0~3.5 μm cubic pixels. Osmium-tetroxide staining of samples after soaking in glutaraldehyde provided greatly improved contrast (Figure 4c, d).

III. RESULTS AND DISCUSSION

A. Axon-dimension Microneedle in Ultra-flexible Array

We successfully fabricated silicon microneedles having the three stress-reducing features predicted by COMSOL simulations: a large angle on the tip, modest tapering on the sidewall, and a wide base (Figure 2) to minimize lateral and angular movement of the stand-alone needles embedded in a soft, thin elastomer. These low-stress features still allowed us to maintain an average diameter of 7 μm over the tip segment, which we hypothesize will mitigate axon damage, demyelination, and collagenous encapsulation. Results from COMSOL simulation illustrated the stress distribution along one individual silicon microneedle under longitudinal and lateral forces. The maximum local stress, which reflect the most fragile point of the structure, along the needle body was compared between different needle shapes. For a cylindrical profile microneedle, high stress is localized around the “foot” (Figure 2, top). For a simple cone profile microneedle, high stress is localized around the “neck”. By introducing a dual-taper (tip and shaft separated), the stress is distributed more evenly across the whole microneedle.

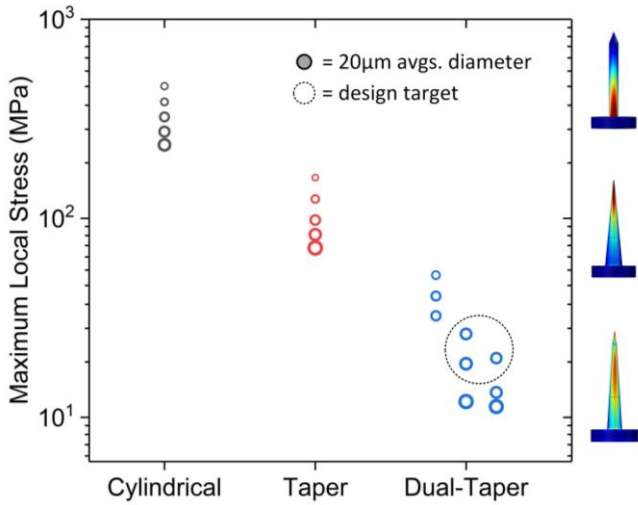


Figure 2. Summary of maximum local stress comparison among different needle shapes. Dot sizes represent the average cross-section diameter. The gray-filled circle in the legend gives a scale bar of 20 μm diameter. Heat maps on needle shapes show where the stress is localized.

The simulation results suggest that more than an order of magnitude maximum stress can be reduced by introducing a

couple of micro-engineered features (Fig. 2). The size of each dot represents a different shaft diameter and angles. Each needle has a total length of 160 μm and a backside anchor base of 20 μm thickness. Three sub-groups for the dual-taper shape (Figure 2, lower right) represent three different shaft angles, 2.5°, 3.5° and 5°. With approximately equal average cross-section diameter at 17.6 μm , a dual-taper shape design (3.5° shaft angle and 15° tip angle) has 20.8 times less maximum stress than cylindrical shape and 7 times less than the simple conical shape. Moreover, the backside anchor structure significantly prevents rotational movement.

Integrated plasma reactor and microneedle scale modeling helped us improve our fabrication process. The model predicted time evolution of profiles defining the needles are shown in Figure 3 (lower right). The first pseudo-isotropic etch step creates a straight angle taper on the cylinder beneath the SiO_2 mask (Figure 3a). As the etching proceeds, the surrounding ring becomes thinner (Figure 3b & c) and is eventually removed (Figure 3d). The gap between the needle and the ring forms a trench with an aspect ratio of 8, which limits the transport of F atoms to the bottom and results in a micro-loading effect. The decreasing height of the surrounding ring during the etching increases access to the central needle by F atoms, eventually trimming the needle shaft from a cylinder into a cone (Figure 3d, f). Experimentally, the first two steps of the plasma etching created the vertical structure shown in in Figure 3a. The last-step isotropic silicon plasma etching process resulted in a profile close to the prediction. The microneedle tip was shaped into an average 13.8° taper while the microneedle body had a 3.3° shaft angle.

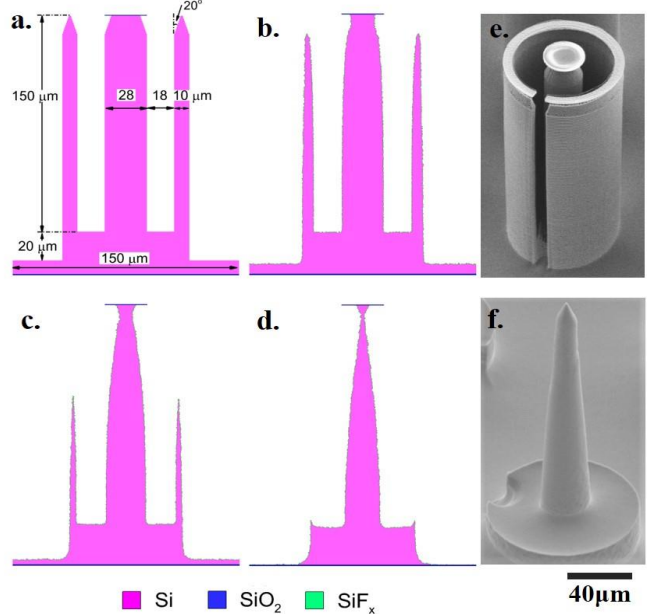


Figure 3. Reactive ion etching model and results. a-d. Time evolution of etching profile during the removal of surrounding rings using ICP sustained in SF_6 at relative time points approximately: $t=0$, 30s, 60s and 90s. e & f. SEM of image of one single structure corresponding to model steps b and d.

B. Implantation and Device-Nerve Adhesion Using Photochemical Bonding

We demonstrate MINA can also be reliably inserted at a higher needle density $61/\text{mm}^2$, compared with the high-density Utah array [9] at $25/\text{mm}^2$, and a flexible penetrating microelectrode array (FPMA) [10] at $3.3/\text{mm}^2$. We have implanted MINA into the rat vagus nerve ($300\text{-}500 \mu\text{m}$) 4 out of 4 times with no observed needle damage or fracture. This robustness of such a fine silicon structure was expected from the short length and tapered shaft (Euler's buckling equation and COMSOL model). While higher density MINA arrays have been fabricated ($100 \mu\text{m}$ pitch) we hypothesize the current pitch of $150 \mu\text{m}$ has a higher likelihood of minimizing tissue reactivity—but this important question should be tested in future work.

During terminal electrophysiology tests (not recorded from MINA) evoked compound action potentials (CAPs) were observed in all implanted nerves, demonstrating that nerves remained functional. Stimulation thresholds for eliciting CAP responses were 1-4 mA. Primary CAP features had conduction velocities of 2.1-6.8 m/s, which aligns with prior recordings from the vagus nerve.

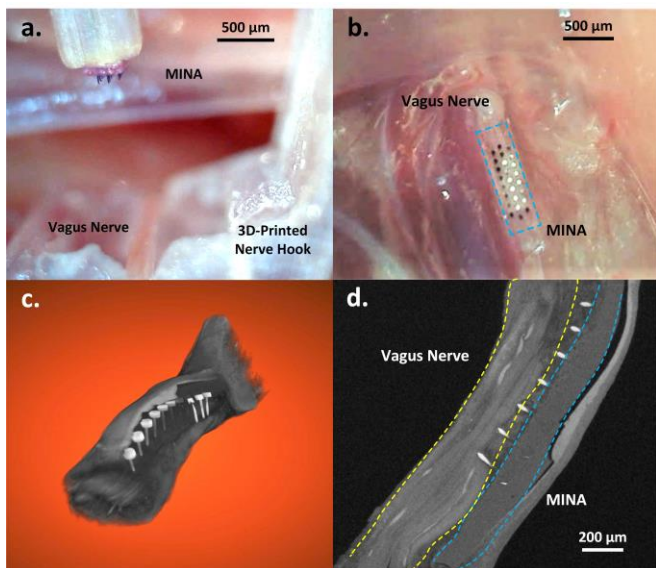


Figure 4. MINA implantation and 1-week time point. a. Top view of MINA and vagus nerve after implantation. b. Side view photo during implantation. c. A reconstructed 3D image from micro-CT showing unbroken needles implanted into the nerve. d. Micro-CT scanned longitudinal nerve section with MINA implanted.

MINA implantation results were investigated through micro-CT imaging. Figure 4b shows the cross-section views of a one-week implanted nerve sample. While some needles are in the nerve, we currently observe epineurium reactivity of connective tissue growth pushes some of the needles out. This may be due to damage from the needles, damage from the laser photochemical activation, or a foreign body reaction. We are currently testing improvements to the insertion process and laser application.

C. Ex vivo Evaluation of Device-Epineurium Adhesion

Similar to our *in vivo* implantation protocol, four freshly explanted rat nerves were implanted with a MINA and placed in a vial of held at either or 50°C for at least 5 weeks. No detachment of MINA was observed during soaking for any samples, providing further evidence this form of photochemical bonding creates a strong nerve-device bonding interface that remains flexible.

IV. CONCLUSION

We demonstrate that axon-dimension needles can be precisely machined and implanted into fine autonomic nerves. We also demonstrate these small, flexible arrays remain on the nerve at a 1-week time point without the use of a cuff. The novel use of Rose Bengal to putatively form thin covalent bonding between a nerve and a sensor array has the advantage of being flexible, unlike cyanoacrylate and other glues. Our future work will demonstrate fully functional arrays and improved surgical techniques.

ACKNOWLEDGMENT

We thank Brian van der Elzen for his expertise on DRIE etching and assistance, Lurie Nanofabrication Facility staffs and Nancy Senabulya at Michigan Center for Material Characterization facilities, University of Michigan. We thank Steve Kemp and Lauren Zimmerman for their advice and assistance with surgical procedures, and Eric Kennedy and the Unit for Laboratory Animal Management.

REFERENCES

- [1] S. Wurth *et al.*, “Long-term usability and bio-integration of polyimide-based intra-neural stimulating electrodes,” *Biomaterials*, vol. 122, p. 114, 2017.
- [2] H. A. C. Wark, K. S. Mathews, R. A. Normann, and E. Fernandez, “Behavioral and cellular consequences of high-electrode count Utah Arrays chronically implanted in rat sciatic nerve,” *J. Neural Eng.*, vol. 11, no. 4, p. 046027, 2014.
- [3] Y. Hanein, C. G. J. Schabmueller, G. Holman, P. Lucke, D. D. Denton, and K. F. Bohringer, “High-aspect ratio submicrometer needles for intracellular applications,” in *Journal of Micromechanics and Microengineering*, vol. 13, no. 4, p. s91, 2003.
- [4] M. J. Kushner, “Hybrid modelling of low temperature plasmas for fundamental investigations and equipment design,” *Journal of Physics D: Applied Physics*, vol. 42, no. 19, p. 194103, 2009.
- [5] C. M. Huard, S. Sriraman, A. Paterson, and M. J. Kushner, “Transient behavior in quasi-atomic layer etching of silicon dioxide and silicon nitride in fluorocarbon plasmas,” *J. Vac. Sci. Technol. A*, vol. 36, no. 6, p. 06B101, 2018.
- [6] A. Lauto *et al.*, “Fabrication and Application of Rose Bengal-chitosan Films in Laser Tissue Repair,” *J. Vis. Exp.*, vol. 68, p. 4158, 2012.
- [7] B. P. Chan, I. E. Kochevar, and R. W. Redmond, “Enhancement of porcine skin graft adherence using a light-activated process,” *J. Surg. Res.*, vol. 108, no. 1, p. 77, 2002.
- [8] N. G. Fairbairn *et al.*, “Light-activated sealing of nerve graft coaptation sites improves outcome following large gap peripheral nerve injury,” in *Plastic and Reconstructive Surgery*, vol. 136, no. 4, p. 739, 2015.
- [9] H. A. C. Wark *et al.*, “A new high-density (25 electrodes/mm²) penetrating microelectrode array for recording and stimulating sub-millimeter neuroanatomical structures,” *J. Neural Eng.*, vol. 10, no. 4, p. 045003, 2013.
- [10] D. Byun, S. J. Cho, B. H. Lee, J. Min, J. H. Lee, and S. Kim, “Recording nerve signals in canine sciatic nerves with a flexible penetrating microelectrode array,” *J. Neural Eng.*, v. 14, no. 4, p. 046023, 2017.